Phase separation in swelling and deswelling hydrogels with a free boundary

Matthew G. Hennessy [1,*] Andreas Münch,[1,†] and Barbara Wagner[2,‡]

[1]*Mathematical Institute, University of Oxford, Andrew Wiles Building, Woodstock Road, Oxford OX2 6GG, United Kingdom*
[2]*Weierstrass Institute, Mohrenstrasse 39, 10117 Berlin, Germany*

We present a full kinetic model of a hydrogel that undergoes phase separation during swelling and deswelling. The model accounts for the interfacial energy of coexisting phases, finite strain of the polymer network, and solvent transport across free boundaries. For the geometry of an initially dry layer bonded to a rigid substrate, the model predicts that forcing solvent into the gel at a fixed rate can induce a volume phase transition, which gives rise to coexisting phases with different degrees of swelling, in systems where this cannot occur in the free-swelling case. While a nonzero shear modulus assists in the propagation of the transition front separating these phases in the driven-swelling case, increasing it beyond a critical threshold suppresses its formation. Quenching a swollen hydrogel induces spinodal decomposition, which produces several highly localized, highly swollen phases which coarsen and are then ejected from free boundary. The wealth of dynamic scenarios of this system is discussed using phase-plane analysis and numerical solutions in a one-dimensional setting.

I. INTRODUCTION

Hydrogels are, in the simplest case, two-phase systems composed of an elastic network of polymer chains immersed in a liquid solvent. The transport of solvent into and out of the network leads to the swelling and drying of the hydrogel, thereby introducing large deformations of the polymer network. Since hydrogels are omnipresent in nature, in innumerable biological processes, but also in many smart soft-matter as well as medical applications, there have been a large number of theoretical and experimental studies aiming at understanding the dynamic behavior and pattern formation during swelling and drying processes [1–9]. Fundamental phenomena include the formation of a core-shell structure for the swelling of beads [1,10], or the appearance of wrinkling instabilities, such as those described in the seminal work by Tanaka *et al.* [11] and others [1,12].

Aside from swelling and deswelling with their large volume changes, polymer gels can exhibit a volume phase transition giving rise to coexisting regions with different degrees of swelling and hence different levels of elastic stresses. The volume phase transition was theoretically predicted [13] and then identified in polyacrylamide gels upon temperature and fluid compositional changes [14], and explored in a host of situations and potential applications. Recently, it was shown that external stimuli such as stretching or compression of the gel can also greatly affect the transition [15]. Sudden quenching of a swollen polymer bead leads to a cloudy appearance, indicating the onset of phase separation *via* spinodal decomposition, followed by growth and expulsion of the solvent-rich domains from the gel [16]. The volume changes induced by this process lead to deformation of the boundary in contact with the surrounding bath as well as a host of patterns within a shrinking gel [17]. The polymer matrix can impede growth of the solvent-rich domains beyond a certain size, which is exploitable for applications: In [18], the authors use this arrested phase separation in a polymer gel to produce droplets of tunable size. The range of new potential applications that explore or exploit the relationship between forced mass transport and heterogeneous microstructures [19], for example in extreme mechanics, have led to a sharp rise in the interest in phase transitions of gels, as documented in the topical review by Dimitriyev *et al.* [20].

While the phenomenon of the volume phase transition has been known for several decades, theoretical treatment has been mainly carried out through thermodynamical equilibrium descriptions with jump conditions at explicit interfaces between the coexisting phases, e.g. [12], and occasional variational approaches. Since the kinetics of swelling and deswelling can change significantly upon the formation of internal interfaces by phase transitions, full time-dependent models that implicitly capture these interfaces are needed.

Phase-field theories provide a natural framework for developing kinetic models of hydrogels by accounting for the relevant thermodynamics as well as providing implicit descriptions of the evolving interfaces that form upon phase separation. Such models have been used to study phase separation in two-dimensional situations without considering the effect of boundaries, i.e., periodic boundary conditions were imposed [21–23]. In Drozdov *et al.* [24] a hydrogel model that accounts for fixed boundaries was formulated but the energy of internal interfaces was not considered.

The focus of this study is to investigate the role of solvent exchange through a free boundary between the bath and the gel in driving the system toward phase separation. We derive our model along the lines of Drozdov *et al.* [24] and extend the classical Flory-Rehner free energy [25] by accounting for

---

*hennessy@maths.ox.ac.uk
†muench@maths.ox.ac.uk
‡barbara.wagner@wias-berlin.de

the gradient-squared terms associated with the interfacial free energy. The governing equations are then derived from the energy imbalance inequality of Gurtin [26]. Accordingly, we formulate appropriate conditions at the fixed boundaries, as well as the free boundaries.

The general three-dimensional free-boundary problem for a hydrogel that allows for solvent exchange through the free boundaries and the formation of internal interfacial layers is presented in Sec. II. In Sec. III we use our model to investigate a hydrogel that is immersed in a solvent bath and allowed to freely swell and compare this to the problem where the hydrogel is forced to swell due to an imposed constant flux of solvent through the free boundary. By combining linear stability analysis with numerical simulation and phase-space analysis of the quasistationary equations in a one-dimensional setting, our model predicts that in the free-swelling case a volume phase transition cannot occur. However, for the forced-swelling case, a dynamic volume phase transition can occur via a propagating front when the Flory-Huggins parameter is above a critical value. In addition, we investigate the effect of quenching a swollen hydrogel and show that spinodal decomposition leads to the formation of several highly localized, highly swollen domains which are ejected from the hydrogel one by one. We summarize our conclusions and give an outlook on future research in Sec. IV.

II. MODELING

When a dry polymer network is immersed in a solvent bath, osmotic forces drive solvent molecules into the network in order to reduce the free energy of mixing. However, the polymer chains must stretch to accommodate the volume of solvent molecules, thereby increasing the elastic energy of the network. Equilibrium is obtained when the energy decrease due to mixing exactly balances the energy cost of deforming the polymer network. Following previous works that exploit the energy-driven nature of swelling [12,24,27–29], we develop a continuum model for a hydrogel based on the thermodynamics of solvent-polymer mixtures. However, we also account for the energy cost of composition gradients, which are typically associated with the energy of internal interfaces that form due to phase separation.

We first present the balance equations representing conservation of mass and momentum in the dry (reference) and swollen (current) configurations. We then construct the free energy of the system and apply the energy imbalance inequality of Gurtin [26] to obtain thermodynamically consistent expressions for the flux, stress, and constitutive relationships. Finally, the boundary conditions for a specific geometry are described.

A. Bulk equations

1. Balance laws

As the hydrogel swells, material elements that are initially located at the (Lagrangian) coordinates $X = (X_1, X_2, X_3)$ are displaced to (Eulerian) points $x = (x_1, x_2, x_3)$. The deformation gradient tensor $\mathbf{F} = \partial x / \partial X$ and its determinant $J = \det \mathbf{F}$, respectively, encode information about how these material elements are distorted and change volume during

swelling. Assuming that the hydrogel is composed of an incompressible polymer network, the increase in volume of a material element must be directly linked to the concentration C of solvent molecules contained within that element. This leads to the molecular incompressibility condition

$$J = 1 + vC, \tag{1}$$

where v is the volume of a solvent molecule. The nominal concentration C describes the number of solvent molecules per unit volume of the dry state. The actual solvent concentration, i.e., the number of solvent molecules per unit volume of the current state, is given by $c = C/J$. The volume fractions of solvent and polymer network can then be defined as $\phi_f = vC/J$ and $\phi_n = 1 - \phi_f = J^{-1}$, respectively.

Conservation of solvent in the dry configuration is given by

$$\dot{C} + \nabla_0 \cdot \boldsymbol{j}_0 = 0, \tag{2}$$

where $\boldsymbol{j}_0$ is the nominal flux, which is defined per unit area in the dry state, and ∇_0 denotes the gradient with respect to the Lagrangian coordinates X. Similarly, conservation of momentum reads as

$$\nabla_0 \cdot \mathbf{S} = 0, \tag{3}$$

where $\mathbf{S}$ is the first Piola-Kirchhoff stress tensor. The corresponding balance laws in the current state are given by (see Appendix A)

$$\frac{\partial c}{\partial t} + \nabla \cdot (c\boldsymbol{v}_n + \boldsymbol{j}) = 0, \tag{4a}$$

$$\nabla \cdot \mathbf{T} = 0. \tag{4b}$$

where $\boldsymbol{v}_n$ is the velocity of the polymer network, $\boldsymbol{j} = J^{-1}\mathbf{F}\boldsymbol{j}_0$ is the flux, $\mathbf{T} = J^{-1}\mathbf{S}\mathbf{F}^T$ is the Cauchy stress tensor, and ∇ denotes the gradient with respect to the Eulerian coordinates x.

2. Construction of the free energy

Constitutive equations that are consistent with the second law of thermodynamics can be derived by considering the Helmholtz free energy per unit volume in the dry configuration ψ. This is composed of four contributions

$$\psi = \psi_1 + \psi_2 + \psi_3 + \psi_4, \tag{5a}$$

corresponding to the energy of solvent not interacting with the solid phase (ψ_1); the energy of the polymer network not interacting with solvent (ψ_2), i.e., the elastic energy of the network; the energy of mixing solvent with the polymer network (ψ_3); and the interfacial energy between the solvent and polymer phases (ψ_4). The first three contributions are given by Drozdov *et al.* [24]:

$$\psi_1 = \mu_0 C, \tag{5b}$$

$$\psi_2 = \mathcal{W}(I_1, I_2, J), \tag{5c}$$

$$\psi_3 = \frac{k_B T}{v} J(\phi_f \ln \phi_f + \chi \phi_f \phi_n), \tag{5d}$$

where μ_0 denotes the chemical potential of a solvent bath, $\mathcal{W}$ is the hyperelastic strain energy (per unit volume in the dry state), I_1 and I_2 are the first and second principal invariants of the right Cauchy-Green tensor $\mathbf{C} = \mathbf{F}^T\mathbf{F}$, k_B is Boltzmann's

constant, T is temperature, and χ is the Flory-Huggins parameter. We will consider an idealized system where χ can be treated as a constant as in Bertrand *et al.* [1] and elaborate on the implications of this assumption in Sec. IV. The final contribution to the free energy ψ_4 is determined by assuming that ideal interfaces [27] form between the two phases, leading to

$$\psi_4 = \frac{\gamma(C)}{2} J \,|\nabla C|^2 = \frac{\gamma(C)}{2} J H_{iK} \frac{\partial C}{\partial X_K} \frac{\partial C}{\partial X_L} H_{iL}. \quad (6)$$

The function γ plays the role of a surface energy and the tensor $\mathbf{H}$ with components H_{iK} is defined as $\mathbf{H} = \mathbf{F}^{-T}$. The concentration dependence of γ enables various forms of the interfacial energy ψ_4 to be captured. For example, $\psi_4 = (\gamma_0/2)J|\nabla c|^2$ can be recast into (6) by setting $\gamma(C) = \gamma_0/(1+C)^4$.

3. Energy imbalance inequality

Having defined the free energy of the mixture, we now proceed to determining the constitutive relationships through the use of the energy imbalance inequality of Gurtin [26]. In essence, this inequality states that the energy gain in every control volume $\mathcal{V}_0$ (of the dry state) is at most equal to the total influx of energy and working combined. The integral form of the inequality is given by

$$\frac{d}{dt} \int_{\mathcal{V}_0} \psi \, dX \leqslant - \int_{\partial \mathcal{V}_0} \mu \boldsymbol{j}_0 \cdot \boldsymbol{N} \, dA$$
$$+ \int_{\partial \mathcal{V}_0} (\boldsymbol{\xi} \cdot \boldsymbol{N}) \dot{C} \, dA + \int_{\partial \mathcal{V}_0} \mathbf{S} \boldsymbol{N} \cdot \dot{\boldsymbol{u}} \, dA, \quad (7)$$

where μ is the chemical potential of solvent in the polymer network, $\boldsymbol{\xi}$ is the microstress, and $\boldsymbol{u} = \boldsymbol{x} - \boldsymbol{X}$ is the displacement vector. Equation (7) must be satisfied for all volume elements $\mathcal{V}_0$. Hence, after using the divergence theorem on the right-hand side, we can localize to obtain

$$\dot{\psi} + \nabla_0 \cdot (\mu \boldsymbol{j}_0) - \nabla_0 \cdot (\boldsymbol{\xi} \dot{C}) - \nabla_0 \cdot (\mathbf{S}^T \cdot \dot{\boldsymbol{u}}) \leqslant 0. \quad (8)$$

By differentiating the incompressibility condition (1) with respect to time, we obtain

$$v\dot{C} - J\mathbf{F}^{-T} : \dot{\mathbf{F}} = 0. \quad (9)$$

By adding (9) times a Lagrange multiplier p to (8) and then using $\psi = \psi(C, \nabla_0 C, \mathbf{F})$ along with the chain rule, we obtain

$$\left(\frac{\partial \psi}{\partial \nabla_0 C} - \boldsymbol{\xi} \right) \cdot \nabla_0 \dot{C} + \left(\frac{\partial \psi}{\partial C} - \mu - \nabla_0 \cdot \boldsymbol{\xi} + pv \right) \dot{C}$$
$$+ \left(\frac{\partial \psi}{\partial \mathbf{F}} - \mathbf{S} - pJ\boldsymbol{F}^{-T} \right) : \dot{\mathbf{F}} + \nabla_0 \mu \cdot \boldsymbol{j}_0 \leqslant 0. \quad (10)$$

As will be shown below, the multiplier p plays the role of the mechanical pressure. The quantities $\nabla_0 \dot{C}$, $\dot{C}$, $\dot{\mathbf{F}}$, and $\nabla_0 \mu$ can be chosen independently at each point $\boldsymbol{X}$ and each time t. In particular, we can keep $\nabla_0 \mu = 0$ and then vary the other three terms individually. Since none of the terms in the brackets depend on any of these three quantities, the only way to satisfy

the inequality in all cases is to assume the brackets vanish identically. Hence, we obtain

$$\boldsymbol{\xi} = \frac{\partial \psi}{\partial \nabla_0 C}, \quad (11a)$$

$$\mu = vp + \frac{\partial \psi}{\partial C} - \nabla_0 \cdot \boldsymbol{\xi}, \quad (11b)$$

$$\mathbf{S} = -pJ\mathbf{F}^{-T} + \frac{\partial \psi}{\partial \mathbf{F}}. \quad (11c)$$

What remains of (10) is then the inequality

$$\nabla_0 \mu \cdot \boldsymbol{j}_0 \leqslant 0, \quad (12)$$

which can be satisfied by choosing the nominal flux to be of the form

$$\boldsymbol{j}_0 = -\mathbf{M}(C, \mathbf{C})\nabla_0 \mu, \quad (13)$$

where $\mathbf{M}$ is a positive-semidefinite mobility tensor.

4. Specification and simplification of constitutive equations

The expressions in (11) can be evaluated to derive explicit expressions for the Cauchy stress $\mathbf{T}$ and the chemical potential μ. We find that

$$\mathbf{T} = -p\mathbf{I} + \frac{1}{J} \frac{\partial \mathcal{W}}{\partial \mathbf{F}} \mathbf{F}^T + \mathbf{K}, \quad (14a)$$

$$\mathbf{K} = \gamma(C)\left(\frac{1}{2}|\nabla C|^2 \mathbf{I} - \nabla C \otimes \nabla C \right), \quad (14b)$$

where $\mathbf{I}$ is the identity tensor. The first term in (14a) describes an isotropic stress induced by the pressure, the second term is the elastic stress of the network, and the final term represents the Korteweg stress generated by internal interfaces. The calculation of the Korteweg stress tensor can be found in Appendix B. We will assume that the elastic response of the polymer network can be described by the neo-Hookean equation of state with shear modulus G:

$$\mathcal{W} = \frac{G}{2}(I_1 - 3 - 2\ln J). \quad (15)$$

Using this in (14a) gives

$$\mathbf{T} = -p\mathbf{I} + \frac{G}{J}(\mathbf{B} - \mathbf{I}) + \mathbf{K}, \quad (16)$$

where $\mathbf{B} = \mathbf{F}\mathbf{F}^T$ is the left Cauchy-Green strain tensor.

The chemical potential μ can be written as

$$\mu = \mu_0 + v(p + \Pi) + \mu_M + \mu_G, \quad (17a)$$

where the mechanical pressure p, osmotic pressure Π, and μ_M and μ_G can be interpreted as the contributions from mechanical stress, mixing, surface-energy gradients, and composition gradients, respectively. The latter three quantities are defined as

$$\Pi = \frac{k_B T}{v}\left[\ln\left(\frac{vC}{1+vC} \right) + \frac{1 + vC + \chi}{(1+vC)^2} \right], \quad (17b)$$

$$\mu_M = \frac{\gamma'(C)}{2} J|\nabla C|^2, \quad (17c)$$

$$\mu_G = -J\nabla \cdot [\gamma(C)\nabla C]. \quad (17d)$$

A derivation of (17d) is provided in Appendix C.

The mobility tensor $\mathbf{M}$ appearing in (13) can be determined by writing the flux in the current configuration as

$$\boldsymbol{j} = -\frac{Dc}{k_B T}\boldsymbol{\nabla}\mu. \tag{18}$$

By transforming (18) into variables associated with the dry state, we find that

$$\boldsymbol{j}_0 = -\frac{DC}{k_B T}\mathbf{C}^{-1}\boldsymbol{\nabla}_0\mu, \tag{19}$$

from which we conclude that

$$\mathbf{M} = \frac{DC}{k_B T}\mathbf{C}^{-1}. \tag{20}$$

It is insightful to examine the form of the flux after (18) has been evaluated using the chemical potential (17). The flux can be decomposed into four contributions associated with distinct driving mechanisms:

$$\boldsymbol{j} = \boldsymbol{j}_1 + \boldsymbol{j}_2 + \boldsymbol{j}_3 + \boldsymbol{j}_4, \tag{21a}$$

$$\boldsymbol{j}_1 = -D\left[\frac{1 + (1 - 2\chi)vC}{(1 + vC)^4}\right]\boldsymbol{\nabla}C, \tag{21b}$$

$$\boldsymbol{j}_2 = -\frac{D}{k_B T}\frac{vC}{1 + vC}\boldsymbol{\nabla}p, \tag{21c}$$

$$\boldsymbol{j}_3 = -\frac{D}{2k_B T}\frac{C}{1 + vC}\boldsymbol{\nabla}[\gamma'(C)(1 + C)|\boldsymbol{\nabla}C|^2], \tag{21d}$$

$$\boldsymbol{j}_4 = \frac{D}{k_B T}\frac{C}{1 + vC}\boldsymbol{\nabla}((1 + vC)\boldsymbol{\nabla}\cdot[\gamma(C)\boldsymbol{\nabla}C]). \tag{21e}$$

The flux vector $\boldsymbol{j}_1$ describes the transport of solvent driven by the osmotic pressure and $\boldsymbol{j}_2$ describes the flux driven by the gradient of the mechanical pressure. Dropping for now $\boldsymbol{j}_3$ and $\boldsymbol{j}_4$ and taking the limit $vC \to 0$, we recover Fick's law of diffusion

$$\boldsymbol{j} = -D\boldsymbol{\nabla}C; \tag{22}$$

conversely, in the limit $vC \to \infty$, we obtain Darcy's law

$$\boldsymbol{j} = -\frac{D}{k_B T}\boldsymbol{\nabla}p. \tag{23}$$

Darcy's law is usually written in the form

$$\boldsymbol{v}_f - \boldsymbol{v}_n = -\frac{\phi_f}{\zeta}\boldsymbol{\nabla}p, \tag{24}$$

where $\boldsymbol{v}_f$ is the velocity vector of the fluid and ζ is a coefficient of friction between solvent molecules and segments of chains. This friction coefficient is experimentally measured to be governed by the law (see, e.g., Drozdov *et al.* [24])

$$\zeta = \zeta_0\phi_n^\beta\phi_f^2, \quad \beta = 1.5. \tag{25}$$

As shown in Appendix A, the flux $\boldsymbol{j}$ is equal to $c(\boldsymbol{v}_f - \boldsymbol{v}_n)$. Therefore, comparing (23) and (24) gives an expression for the diffusivity,

$$D = D_0(1 + vC)^\beta, \tag{26}$$

where $D_0 = (k_B T)/(\zeta_0 v)$.
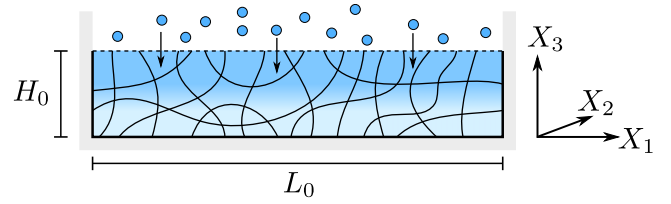
FIG. 1. Schematic of the cross section of a laterally bounded gel film that is attached to a rigid substrate (shown here in the reference state). The gel can exchange solvent with a bath through its upper surface.

B. Boundary conditions

To facilitate the discussion of boundary conditions, we consider a specific geometry based on a thin film of hydrogel that is bonded to a rigid substrate, as shown in Fig. 1. The upper surface of the hydrogel is in contact with a solvent bath. We consider an idealized situation whereby the sides of the hydrogel are held into position so that lateral expansion is not possible. Although the boundary conditions that apply at the substrate and sides are specific to this geometry, the conditions at the bath-gel interface are general and can be applied to other systems, e.g., spherical hydrogel beads immersed in a solvent bath.

1. Boundary conditions at the substrate

At the bottom surface, $X_3 = 0$ (or $x_3 = 0$), the hydrogel film is attached to a rigid substrate. We therefore impose no-displacement conditions

$$\boldsymbol{u} = 0. \tag{27}$$

Moreover, the flux of solvent vanishes, as the substrate is assumed to be impenetrable,

$$\boldsymbol{j} \cdot \boldsymbol{e}_3 = 0, \tag{28}$$

where $\boldsymbol{e}_i$ are the canonical unit vectors (in the current configuration). A further boundary condition is needed since second-order derivatives of C appear in the expression for the chemical potential μ. We use the condition

$$\boldsymbol{\nabla}C \cdot \boldsymbol{e}_3 = 0, \tag{29}$$

which describes a situation where the gel is in local equilibrium with a neutral wall, that is, a wall that does not have a preference for either the gel or the solvent. This is a special case of the boundary conditions used for phase-field models in the context of surface-directed phase separation, e.g., [30]. The ramifications of prescribing the concentration gradient will be discussed in greater detail below; however, we mention here that (29) can lead to boundary layers as γ becomes small.

2. Boundary conditions at the side walls

At the side walls, $X_1 = 0, L_0$, and $X_2 = 0, L_0$, the gel cannot move sideways but may slide freely along these walls, hence, we impose

$$\boldsymbol{u} \cdot \boldsymbol{e}_k = 0, \quad \boldsymbol{e}_3 \cdot \mathbf{T} \cdot \boldsymbol{e}_k = 0, \tag{30}$$

where $k = 1, 2$. Again, we assume no flux

$$\boldsymbol{j} \cdot \boldsymbol{e}_k = 0, \tag{31}$$

and adopt the additional boundary condition

$$\nabla C \cdot \boldsymbol{e}_k = 0. \tag{32}$$

3. Boundary conditions at the bath-gel interface

The bath-gel interface is located at $X_3 = H_0$ in the dry state or $x_3 = h(x_1, x_2, t)$ in the current state, where H_0 denotes the initial thickness of the polymer network. The normal vector to the bath-gel interface in the current configuration is denoted by $\boldsymbol{n}$, which points from the gel into the bath.

The solvent bath is assumed to be stress free. This means we essentially assume a hydrostatic situation without a body force (e.g., gravity), giving constant pressure in the bath. The constant is free so we simply set it to zero. Continuity of stress across the bath-gel interface then leads to

$$\mathbf{T} \cdot \boldsymbol{n} = 0. \tag{33}$$

We consider two possible boundary conditions describing the transport of solvent across the bath-gel interface. In the first, local chemical equilibrium across this interface in imposed. This requires the chemical potential of solvent in the gel and in the bath to be equal, so that

$$\mu = \mu_0. \tag{34}$$

Alternatively, a prescribed solvent flux Q into the hydrogel can be imposed [31],

$$\boldsymbol{j} \cdot \boldsymbol{n} = -Q, \tag{35}$$

which can be experimentally realized through the use of a syringe [19]. We refer to (34) and (35) as free-swelling and forced-swelling conditions, respectively. The free-swelling condition (34) is frequently used in hydrogel models that do not account for the energy cost of composition gradients, and it leads to a scenario whereby the gel freely swells until an equilibrium is established between mixing and elasticity. In the forced-swelling case described by (35), the solvent concentration can be pushed beyond its equilibrium value, allowing for greater exploration of the energy landscape. A forced influx of solvent cannot be sustained indefinitely, however, as this could stretch the polymer chains beyond their extensibility limit or lead to rupturing of the gel.

As with the other boundaries, we also impose

$$\nabla C \cdot \boldsymbol{n} = 0 \tag{36}$$

at the bath-gel interface. Interestingly, the normal component of the concentration gradient at a free or fixed boundary controls the tangential Korteweg stresses. Setting the normal concentration gradient to zero, as done here, eliminates these stresses.

III. PHASE SEPARATION IN A HOMOGENEOUS GEL

We consider a one-dimensional swelling scenario in which the hydrogel undergoes uniaxial deformations of the form $\mathbf{F} = \mathrm{diag}(1, 1, J)$. This one-dimensional approximation is valid when the lateral dimensions of the gel L_0 are either large [12] or small compared to its height h. The former case may lead to the onset of instabilities, as discussed in Sec. IV; the latter case may be difficult to achieve in experiments due to friction at the side walls which is neglected in the model. It is

convenient to formulate the one-dimensional model in terms of the Lagrangian coordinates associated with the dry state because this removes the need to track the free boundary at $x_3 = h(t)$. For convenience, we relabel the vertical coordinate X_3 as Z. It is assumed that all of the variables only depend on Z and time t. The corresponding balance equations are given by

$$\partial_t C + \partial_Z j_0 = 0, \tag{37a}$$

$$\partial_Z \mathsf{S}_{33} = 0, \tag{37b}$$

where the vertical components of the nominal stress tensor and flux are

$$\mathsf{S}_{33} = -p + \frac{G}{1 + vC}[(1 + vC)^2 - 1] - \frac{\gamma(C)}{2}\frac{(\partial_Z C)^2}{(1 + vC)^2}, \tag{38}$$

$$\begin{aligned}
j_0 = -D_0(1 + vC)^{\beta-2}C\Bigg\{ &\left[\frac{1 + (1 - 2\chi)vC}{C(1 + vC)^3}\right]\partial_Z C \\
&+ \frac{v}{k_B T}\partial_Z p + \frac{1}{2k_B T}\partial_Z\left[\frac{\gamma'(C)}{1 + vC}(\partial_Z C)^2\right] \\
&- \frac{1}{k_B T}\partial_Z^2\left(\frac{\gamma(C)\partial_Z C}{1 + vC}\right)\Bigg\}. \tag{39}
\end{aligned}$$

The vertical stress balance (37b) can be integrated and the stress-free condition at the free surface used to show that $\mathsf{S}_{33} = 0$, which from (38) provides an expression for the pressure p:

$$p = \frac{G}{1 + vC}[(1 + vC)^2 - 1] - \frac{\gamma(C)}{2}\frac{(\partial_Z C)^2}{(1 + vC)^2}. \tag{40}$$

The horizontal components of the stress tensor are

$$\mathsf{S}_{11} = \mathsf{S}_{22} = -G[(1 + vC)^2 - 1] + \frac{\gamma(C)}{1 + vC}(\partial_Z C)^2, \tag{41}$$

showing that the gel can experience a net compressive stress that can result in instability (see, e.g., [32,33]). Using the pressure (40), the flux (39) can be formulated in terms of the concentration and its gradients, thus reducing the model to a single equation for C. Before presenting this equation, it is convenient to nondimensionalize the model as follows:

$$z = H_0 z^*, \quad t = \frac{H_0^2}{D_0}t^*, \quad j_0 = \frac{D_0}{H_0 v}j^*, \tag{42a}$$

$$\mathbf{S} = G\mathbf{S}^*, \quad p = Gp^*, \quad C = v^{-1}C^*, \tag{42b}$$

$$\gamma(C) = \gamma_0\gamma^*(C^*), \quad \mu = \mu_0 + k_B T\mu^*, \tag{42c}$$

and define the nondimensional parameters

$$\mathcal{G} = \frac{Gv}{k_B T}, \quad \omega = \frac{v}{k_B T}\frac{\gamma_0}{v^2 H_0^2}. \tag{43}$$

The parameter $\mathcal{G}$ represents the effective stiffness of the polymer network and it characterizes the ratio of the elastic energy to the mixing energy. Similarly, ω is defined as the ratio of the interfacial energy to the mixing energy and it selects the width of the diffuse interfaces that form when phase separation occurs. The resulting nondimensional problem for

the solvent concentration is, after dropping the star notation and some algebraic manipulation, given by

$$\partial_t C = -\partial_Z j_0, \tag{44a}$$

$$j_0 = -(1+C)^{\beta-2} C \partial_Z \left[F(C) - \frac{\omega}{2} \frac{\gamma'(C)}{(1+C)} (\partial_Z C)^2 \right.$$
$$\left. - \omega \frac{\gamma(C)}{(1+C)^{1/2}} \partial_Z \left(\frac{\partial_Z C}{(1+C)^{1/2}} \right) \right], \tag{44b}$$

$$F = \ln\left(\frac{C}{1+C} \right) + \frac{1+C+\chi}{(1+C)^2} + \mathcal{G} C \left(\frac{2+C}{1+C} \right). \tag{44c}$$

The function F defined in (44c) plays a particularly important role in the model, as it corresponds to the (nondimensional) chemical potential of a homogeneous state; its functional form arises from the mixing and elastic energy densities and can be obtained by differentiating the sum of these contributions with respect to the nominal concentration.

The nondimensional free- and forced-swelling conditions at $Z = 1$ are given by

$$\mu = 0, \tag{45a}$$

$$j_0 = -\mathcal{Q}, \tag{45b}$$

respectively. Here, $\mathcal{Q} = QH_0 v/D_0$ is a dimensionless solvent flux. We also impose $j_0 = 0$ at $Z = 0$, $\partial_Z C = 0$ at $Z = 0$ and $Z = 1$, and $C = 0$ when $t = 0$.

A. Equilibrium conditions for a free-swelling gel

The equilibrium states of a freely swelling hydrogel can be determined by seeking a stationary homogeneous solution to (44) of the form $C(Z, t) = C_{\text{eq}}$ with $j_0(Z, t) = 0$. The spatially uniform chemical potential is given by $\mu = F(C_{\text{eq}})$. Thus, from the free-swelling boundary condition (45a), the homogeneous equilibrium concentration of solvent can be obtained from solving the nonlinear equation $F(C_{\text{eq}}) = 0$, which represents a balance between the osmotic and mechanical pressures (or, equivalently, the mixing and elastic energies). Thus, for fixed values of $\mathcal{G}$, the solutions to $F(C_{\text{eq}}; \chi) = 0$ define the homogeneous states on the phase diagram which are in equilibrium with the solvent bath. As shown in Fig. 2 for the case $\mathcal{G} = 0.01$, this curve is monotonic, implying that only a single equilibrium state exists for a given value of χ, and thus a volume phase transition is not possible. A phase-plane analysis below will confirm that this is the case for all values of $\mathcal{G}$ and that nonhomogeneous equilibria are not possible for the free-swelling case.

B. Onset of phase separation: Linear stability analysis

A simple normal modes analysis about a homogeneous state $\bar{C}$ using the ansatz

$$C(Z, t) = \bar{C} + \delta\tilde{C} \exp(\lambda t + iKZ) \tag{46}$$

shows that perturbations will grow at a rate given by

$$\lambda = -(1+\bar{C})^{\beta-2} \bar{C} \left[F'(\bar{C})K^2 + \frac{\omega\gamma(\bar{C})}{1+\bar{C}} K^4 \right], \tag{47}$$

where $F' = dF/dC$ and K is the wave number of the perturbation as measured from the dry state (with $k = J^{-1}K$ denoting
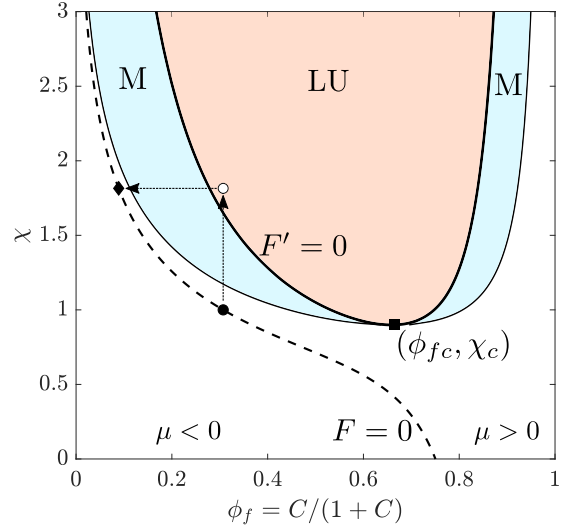
FIG. 2. The phase diagram when $\mathcal{G} = 0.01$ in terms of dimensionless quantities. The dashed line defined by $F = 0$ determines the equilibrium solvent fraction for the free-swelling case as a function of χ. For values of (ϕ_f, χ) to the right of this curve, spatially homogeneous states have a positive chemical potential $\mu = F(C; \chi, G) > 0$, and negative to the left. The thick black line given by $F' = dF/dC = 0$ represents the spinodal curve and marks the boundary of the region where homogeneous states are linearly unstable (LU; shaded red). The thin black lines are defined by (49) and represent the binodal curves. The metastable region (M) is shaded in blue.

the actual wave number). From this we immediately see that the homogeneous state is linearly unstable and the gel layer phase separates if $F'(\bar{C}) < 0$ is fulfilled. The critical case $F'(\bar{C}, \chi) = 0$ defines points on a spinodal curve, which has a minimum at (ϕ_{fc}, χ_c), where

$$\chi_c = \min_{\bar{C} > 0} \frac{(1+\bar{C})[\mathcal{G}(\bar{C}^3 + 2\bar{C}^2 + 2\bar{C}) + 1]}{2\bar{C}}, \tag{48}$$

and $\phi_{fc} = \bar{C}/(1+\bar{C})$ for the $\bar{C}$ where this minimum is achieved, as shown in Fig. 2. We note for future reference that $\chi_c \geq \frac{1}{2}$. Equation (48) shows that increases in the elastic constant $\mathcal{G}$ will shift the spinodal upward, meaning that points initially within the unstable region can become excluded. Thus, the elasticity of the network has the potential to completely suppress the onset of phase separation. The critical value of the elastic constant $\mathcal{G}_c$ at which phase separation is suppressed at a given value of χ can be obtained through the inversion of (48).

The binodal curves $C_1(\chi)$ and $C_3(\chi)$ can be computed using the Maxwell construction, i.e., by solving the nonlinear system

$$\int_{C_1}^{C_3} [F(C) - \bar{\mu}] \, dC = 0, \tag{49a}$$

$$F(C_1) = \bar{\mu}, \quad F(C_3) = \bar{\mu}, \tag{49b}$$

which uniquely determines $\bar{\mu}$, C_1, and C_3 for given χ (and given $\mathcal{G}$). These solutions define the concentrations and hence also the liquid volume fractions of coexisting phases at a phase transition. Notice that (49) only has a solution for $\chi > \chi_c$ and

is equivalent to the common tangent construction since F is the derivative of the homogeneous free energy.

A dry, unswollen gel in ambient conditions will have a chemical potential that is less than zero. Upon immersing this gel in a solvent bath, the surface chemical potential increases to zero. The gradient in chemical potential from the surface to the bulk drives solvent into the gel until the chemical potential is uniformly equal to zero, at which point equilibrium is obtained. From Fig. 2, it is clear that during the free-swelling process, the system is always below or at the curve $F = 0$ and hence no phase transition can occur.

One possible method to induce a phase transition that was explored by Hu *et al.* [16] is by quenching the system via a sudden increase in χ through increasing the temperature. In Fig. 2, we consider an increase from $\chi = 1$ to $\chi = 1.82$. During the increase, which is assumed to be instantaneous, the gel retains a homogeneous solvent distribution with a volume fraction ϕ_f given by $F = 0$ for $\chi = 1$. Immediately after the increase, the system is in the linearly unstable region (marked by an open circle) and has a positive chemical potential. Hence, spinodal decomposition sets in. Over time, however, the system will relax back into equilibrium with the bath, which is at $\mu = 0$, and evolve into the homogeneous state indicated by the solid diamond in Fig. 2.

A second possibility, and the main focus of our numerical experiments in the next section, is by *driving* solvent into the gel, say at a fixed rate. This creates situations with a positive chemical potential in the gel, effectively moving it into the upper-right regions of Fig. 2, enabling phase transitions to occur.

C. Numerical solutions

Numerical simulations are used to study the onset of surface-induced phase separation and the interplay of nonlinear elasticity. The numerical method is based on a finite difference scheme that uses a staggered grid. The flux j_0 is solved on cell edges while the concentration C and the contribution to the chemical potential from the gradient-energy terms μ_G are solved on cell midpoints. A semi-implicit method is used that treats nonlinear terms explicitly and linear terms implicitly. Thus, each time step requires the solution of a linear system of equations for C, j_0, and μ_G. The discretized equations are formulated in terms of Lagrangian coordinates, which fixes the position of the free boundary for the hydrogel surface to $Z = 1$.

For the simulations we set the permeability exponent to $\beta = 0$, the dimensionless surface-energy parameter to $\omega = 10^{-6}$, and use a constant value for the dimensionless surface-energy function $\gamma(C) \equiv 1$. Although our choice of β is smaller than the experimentally measured value, this parameter does not affect the thermodynamics of the system so the qualitative behavior of the solutions should remain the same in all cases. A similar statement holds for ω and $\gamma(C)$, as these quantities mainly control the width of the diffuse interface that forms between coexisting phases. Taking γ as a constant has computational advantages, as it prevents the diffuse interface from becoming extremely thin, which can happen if the decreasing function $\gamma(C) = (1 + C)^{-4}$ associated with the

$|\boldsymbol{\nabla}c|^2$ form of the interfacial energy ψ_4 is used, as discussed in Appendix D.

We first consider a forced-swelling situation by imposing (45b). Due to volume conservation, the thickness of the hydrogel layer grows linearly in time according to $h(t) = 1 + \mathcal{Q}t$. In order to isolate the mechanism of phase separation, the dimensionless solvent flux is set to be $\mathcal{Q} = 0.01$. Larger values of $\mathcal{Q}$ lead to the formation of solvent-rich layers near the free surface even when the thermodynamics of the system do not allow for phase separation. In this case, the formation of solvent-rich layers is due to the vastly different timescales of solvent intake and diffusive mass transport, the former of which is fast compared to the latter. For small values of the flux $\mathcal{Q}$, the concentration of solvent is roughly uniform due to relatively high rate of diffusion, and remains this way until phase separation occurs. In the numerical simulations, the Flory-Huggins parameter is set to $\chi = 1$. This value is based on measurements of the interaction parameter for PHEMA-water and PNIPAM-water gels, which are known to exhibit phase transitions. A composition-dependent quadratic form of χ for PHEMA-water gels is given in Ref. [15] and varies between 0.4 and 1.3. The temperature and concentration dependence of χ for PNIPAM-water has been measured in Ref. [34] and has a maximum value of $\chi = 0.82$ at the phase-transition temperature 305.5 K. As we have neglected the composition dependence of the interaction parameter, larger values of $\chi > \chi_c$ are needed to induce phase separation in our model compared with some experimental systems. The effective elastic constant $\mathcal{G}$ is set to 0, 0.01, 0.02, and 0.05, corresponding to relatively stiff hydrogels with shear moduli on the order of a few MPa (assuming water is the solvent and a temperature of 300 K). For this value of χ, the system exhibits a miscibility gap when $\mathcal{G} \leqslant \mathcal{G}_c = 0.019$. Profiles of the solvent volume fraction ϕ_f are shown in Fig. 3 as functions of the Lagrangian coordinate $\bar{Z} = 1 - Z$ at various times.

In the absence of elastic effects, $\mathcal{G} = 0$ [Fig. 3(a)], the system undergoes phase separation at $t \simeq 73$, forming a highly solvent-rich layer near the hydrogel surface ($\bar{Z} = 0$) and a solvent-poor layer in the bulk. The solvent-rich and solvent-poor layers are separated by a thin interfacial region centered about $\bar{Z} = \bar{S}(t)$, which propagates very slowly into the bulk. The position of the interfacial layer can be implicitly defined by the expression

$$\phi_f(\bar{S}(t), t) = 0.6, \tag{50}$$

and is shown as a function of time in Fig. 4(a). The finite time at which $\bar{S}$ begins to increase from zero marks the onset of phase separation. Interestingly, Fig. 3(a) shows there is a backflow of solvent from the bulk into the surface layer, which causes the surface concentration to increase at the expense of the bulk concentration. Figure 4(b), which plots the evolution of the solvent fraction at the surface of the hydrogel and the substrate, illustrates this more clearly.

When the effective elastic constant is increased to $\mathcal{G} = 0.01$ [Fig. 3(b)], the dynamics remains qualitatively similar. However, the onset of phase separation is slightly delayed and occurs at $t \simeq 79$. Furthermore, the interfacial layer separating the solvent-rich and solvent-poor layers now propagates much more rapidly into the bulk and reaches the substrate when
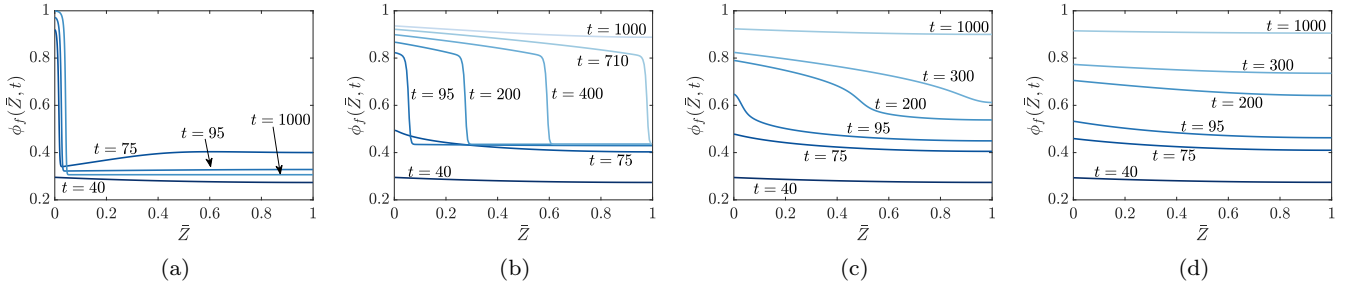
FIG. 3. Numerical simulations of the full model (44) showing the onset and suppression of surface-induced phase separation for weak elasticity and strong elasticity, respectively. The dimensionless shear moduli are given by (a) $\mathcal{G} = 0$, (b) 0.01, (c) 0.02, and (d) 0.05. The parameter values are $\chi = 1$, $\omega = 10^{-6}$, $\beta = 0$, and $\mathcal{Q} = 0.01$. The system has a miscibility gap when $\mathcal{G} \leqslant 0.019$.

$t \simeq 709$, which is shown in Fig. 4(a). Contrary to the inelastic case, there is no backflow of solvent. Once phase separation begins to occur, the concentration of solvent in the bulk (i.e., ahead of the solvent-rich layer) remains constant in time; see Fig. 4(b).

Increasing the effective elastic constant to $\mathcal{G} = 0.02$ prevents the system from exhibiting a miscibility gap [$F'(C) > 0$ for all solvent concentrations]. However, the simulation results in Fig. 3(c) indicate that the system can weakly separate into a solvent-rich and solvent-poor layer, which now occurs at $t \simeq 91$. Unlike the previous two cases, the interfacial region separating the solvent-rich and solvent-poor layers is now much more diffuse. Furthermore, the solvent content ahead of the propagating layer increases in time [see Fig. 4(b)]. As a result, the solvent-rich layer is able to penetrate the depth of the hydrogel and reach the substrate much faster than when $\mathcal{G} = 0$ or 0.01 [see Fig. 4(a)]. When the effective elastic constant is increased to $\mathcal{G} = 0.05$ [Fig. 3(d)], the solvent concentration remains roughly uniform during the entire swelling process.

The numerical simulations show that while elasticity can delay or even suppress the onset of phase separation, it facilitates the propagation of solvent-rich layers into the bulk. The mechanism behind this enhancement is stress-assisted diffusion. The solvent-rich layer will experience a greater degree of volumetric expansion than the solvent-poor layer and hence also experience a greater elastic stress. This gradient in the elastic stress will promote the transport of solvent to the

interfacial layer. As the effective elastic constant increases, this transport becomes so effective that the interfacial layer is suppressed and the composition remains spatially uniform during the entire swelling process.

In cases where phase separation does occur upon initial forcing of solvent into the gel, as in Fig. 3(b), the propagation of the front slowly comes to a rest and the solvent profile approaches an equilibrium shape if the influx of solvent is stopped. This is shown in Fig. 5(a), where the forced-swelling condition (45b) is replaced with a no-flux condition ($\mathcal{Q} = 0$) at time $t = 200$. Hence, the solvent distribution achieved by forced phase separation is long-time stable if the total amount of solvent is conserved. If instead of a no-flux boundary condition being imposed at $t = 200$, the free-swelling condition (45a) is imposed as in Fig. 5(b), then liquid drains back into the bath, forming an advancing depletion front that moves forward as the liquid is removed.

The front is remarkably robust and, as can be seen in Fig. 5(a), persists even after the influx has been stopped, in which case the transition front becomes stationary. The gel composition to the left and right of the front is determined by the binodals (49) as discussed in the section on the phase-plane analysis. The mechanical pressure is larger in the solvent-rich layer and smaller in the solvent-poor layer, whereas the osmotic pressure varies in the opposite manner. When both pressures are summed along with the small
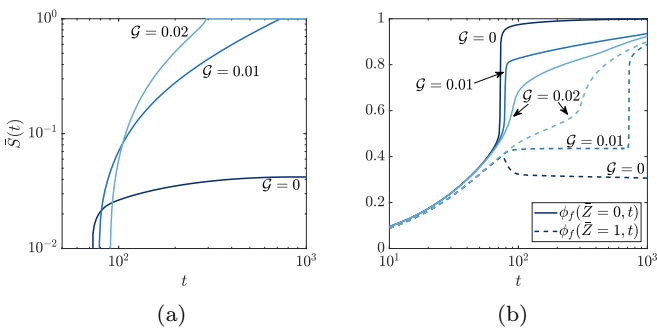
FIG. 4. Evolution of the (a) position of the interfacial layer $\bar{Z} = \bar{S}(t)$ that separates solvent-rich and solvent-poor layers in the hydrogel and (b) the solvent volume fraction at the surface ($\bar{Z} = 0$) and substrate ($\bar{Z} = 1$). The position of the interfacial layer is implicitly defined in (50). The parameter values are $\chi = 1$, $\omega = 10^{-6}$, $\beta = 0$, and $\mathcal{Q} = 0.01$.
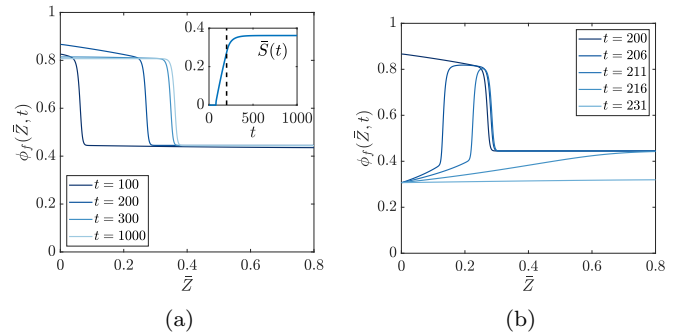
FIG. 5. The effect of stopping the flux of solvent into the gel. Parameters and conditions are the same as for Fig. 3(b) except that the flux was stopped at $t = 200$. In (a), the phase separation solvent profile settles into an equilibrium shape with a fixed front $\bar{S}(t)$. In (b), a constant chemical potential $\mu = 0$ is imposed as a boundary condition at $x = 0$ for $t \geqslant 200$. A second, depletion front forms as the liquid drains out of the gel into the bath at $x = 0$.
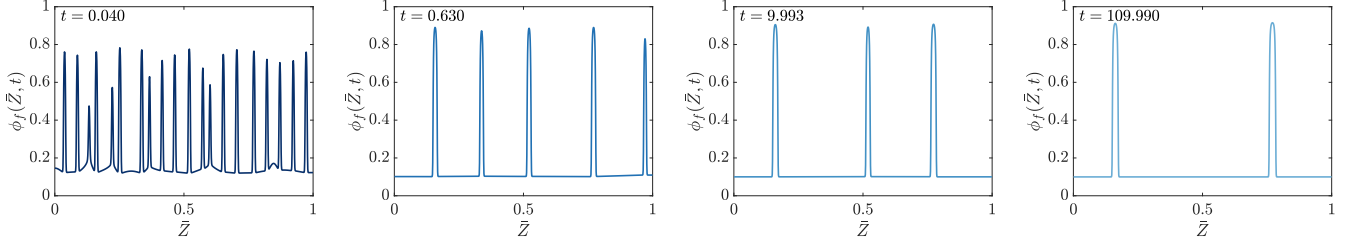
FIG. 6. Phase separation upon quenching a swollen hydrogel with a no-flux boundary condition imposed at the free surface $\bar{Z} = 0$. The initial condition is a noisy homogeneous state calculated with $\chi = 1$. Simulations are carried out at $\chi = 1.82$ with $\omega = 10^{-6}$, $\beta = 0$, and $\mathcal{G} = 0.01$. The initial exponential growth of the perturbations gives way to progressively slower coarsening resulting in a state with two spikes for which no further motion could be detected. Further details are given in the main text.

contribution from μ_G, the chemical potential becomes spatially uniform and takes the value $\mu \simeq 6.57 \times 10^{-2}$. In the case of Fig. 3(a), the elasticity of the network has been neglected so the mechanical pressure is too weak to counterbalance the osmotic pressure. This imbalance drives fluid from the solvent-poor to the solvent-rich layer.

Phase separation can also be induced by quenching, that is, by a sudden change of the temperature that is manifested through a change of χ. We consider a gel that is in equilibrium with a reservoir at $\mu = 0$, then sealed from the bath while the value of χ is dramatically increased. Hence, we start the simulations by first computing the equilibrium concentration associated with $\chi = 1$ by solving $F(C_{\text{eq}}) = 0$ and then perturbing it with small-amplitude random noise. More specifically, the initial concentration is computed by adding a random vector with uniformly distributed entries that lie in the interval $(0, 10^{-4})$ to C_{eq}. The simulations are run with no-flux boundary conditions and a value of $\chi = 1.82$, which leads to $F' < 0$. The results are shown in Fig. 6 for the case of $\mathcal{G} = 0.01$. The onset of phase separation leads to the formation of highly localized solvent-rich regions, and gives rise to a composition profile consisting of several "spikes." The spacing between emerging spikes coincides with the wavelength of the fastest-growing linearly unstable mode that is computed by maximizing (47), which indicates that the initial number of spikes is controlled by the characteristics of the instability. Coarsening then occurs by shrinking some of the spikes, whereby solvent is transferred predominantly to the two immediate neighhors. The state shown in the last subfigure with two spikes is very close to being stationary. There was no visible change up to $t = 1000$ and the typical flux in the domain at this time was approximately 10^{-12}. To ensure the spike solutions are well resolved, we performed simulations using 10^4 grid points, which amounts to roughly 200 grid points per spike.

In Fig. 7, we use the same construction as in Fig. 6 but keep the chemical potential at the free boundary equal to zero, $\mu = 0$, allowing the gel to freely exchange solvent with an adjacent reservoir. Furthermore, we do not perturb the initial composition with random noise. This corresponds to the situation indicated by arrows in Fig. 2. Increasing χ reduces the equilibrium solvent concentration and results in a depletion region that propagates toward the bulk from the free surface. However, in contrast to Fig. 5(b), the depletion front now triggers the onset of phase separation, which occurs in a localized region that grows toward the bulk. The eventual

amplification of fluctuations in the bulk leads to a composition profile that again consists of several spikes with high solvent content. During the coarsening process, the solvent in the spikes that are closer to the free surface tends to be rejected from the network sooner and the spikes that are deeper in the bulk persist for longer. After a sufficient amount of time has passed, all excess solvent is pushed into the reservoir and a homogeneous final state is recovered (not shown here).

The coarsening events are easily detected as kinks in the evolution of the gel thickness,

$$h(t) = 1 + \int_0^1 C(Z, t) \, dZ. \tag{51}$$

Each kink marks a change in the rate at which the hydrogel thins. This decrease occurs because coarsening continually diminishes the gradient in the chemical potential and, consequently, the driving force behind solvent transport to the free surface. After the final coarsening event, the thickness of the network has decreased to 76% of its initial swollen value. This situation is qualitatively similar to the experiment by Hu *et al.* [16], who report highly swollen domains being ejected from hydrogels that have undergone phase separation and are surrounded by a solvent bath.

D. Phase-plane analysis

We investigate the structures seen in the simulations further *via* a phase-plane analysis of the quasistationary solutions for negligible flux. Thus, making the simplifications $\dot{C} \ll 1$ and $j_0 \ll 1$ in (44), as well as $\gamma(C) \equiv 1$ for consistency with the simulations, leads to the conclusion that the chemical potential μ is uniform and the concentration must satisfy the second-order ordinary differential equation (ODE)

$$\omega \, \partial_Z \left(\frac{\partial_Z C}{(1 + C)^{1/2}} \right) = (1 + C)^{1/2} [F(C) - \mu], \tag{52}$$

where F is defined in (44c). The generalized case with $\gamma = \gamma(C)$ is discussed in Appendix D. The equivalent phase-plane system is given by

$$\partial_Z C = (1 + C)^{1/2} W, \tag{53a}$$

$$\partial_Z W = (1 + C)^{1/2} [F(C) - \mu]. \tag{53b}$$

Notice that we have tacitly rescaled Z by $\omega^{1/2} \ll 1$. This ODE system has fixed points, i.e., constant solutions, $(C, W) = (C_e, 0)$ where $F(C_e) - \mu = 0$, and these are saddle points if
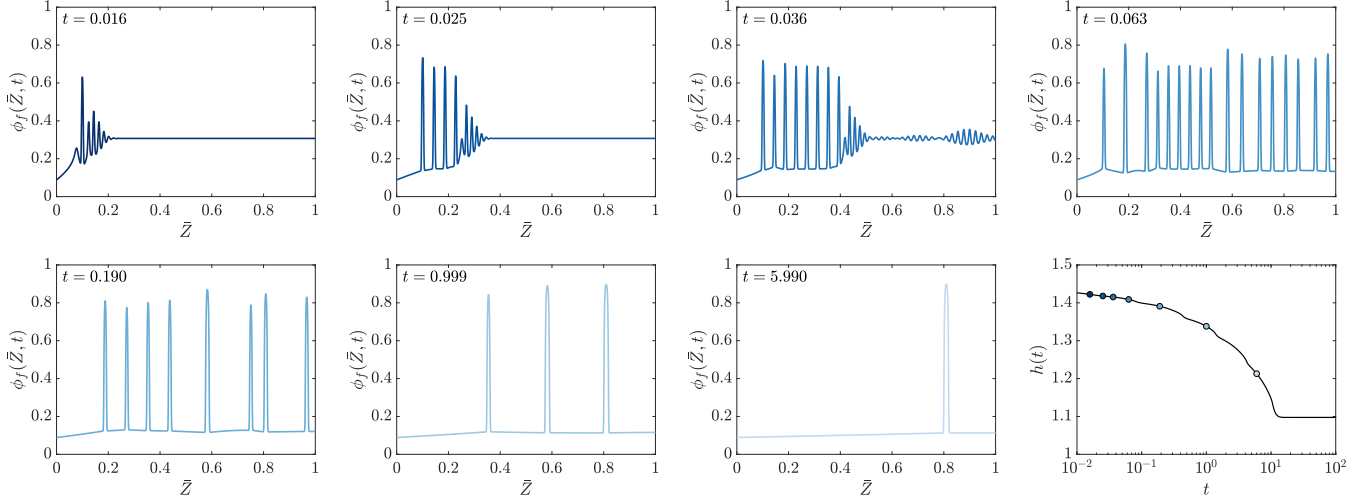
FIG. 7. Phase separation upon quenching a swollen hydrogel with the boundary condition $\mu = 0$ imposed at the free surface $\bar{Z} = 0$. The initial condition is the homogeneous equilibrium solution at $\chi = 1$ (without noise). Simulations are carried out using $\chi = 1.82$ with $\omega = 10^{-6}$, $\beta = 0$, and $\mathcal{G} = 0.01$. The penultimate image is not the final state, as the single peak eventually vanishes.

$F'(C_e) > 0$ or centers if $F'(C_e) < 0$, near which solutions are periodic since the system has a first integral (the total energy of the system).

The number of fixed points depends on the value of μ and the shape of the graph of F. Figure 8(a) shows graphs of F for $\chi = 1$ (this will be our value in the following unless otherwise stated) and the four different values of $\mathcal{G}$ used in the numerical simulations in previous sections. The value of χ was chosen to be larger than $\frac{1}{2}$, which is the critical χ_c without elasticity ($\mathcal{G} = 0$). We expect the system to stabilize for sufficiently large $\mathcal{G}$ and find, for $\chi = 1$, that above $\mathcal{G}_c = 1.86 \times 10^{-2}$, all homogeneous gel compositions are stable, i.e., there is no miscibility gap. We can see that we have either one, two, or three fixed points, depending on the values of $\mathcal{G}$ and μ.

For $\mathcal{G} = 0.05 > \mathcal{G}_c$, the function F increases monotonically and hence we have only one fixed point C_1, which is a saddle. Inspection of the phase plane in Fig. 8(b) shows that the only solution of (52) with boundary conditions $\partial_Z C = 0$ at $Z \to \pm\infty$ is the constant solution $C = C_1$. Hence, forced solutions of the time-dependent problem which are quasistationary due to small influx are almost flat, i.e., only slightly perturbed constant solutions as in Fig. 3(d). Since $\mathcal{G} = 0.02$ is also above $\mathcal{G}_c$, the situation is the same for Fig. 3(c), though at early times, the deviations from flat states are larger as we are closer to the critical value of $\mathcal{G}$.

We note that for $\mu = 0$, we obtain this phase plane situation for all non-negative $\mathcal{G}$ and χ. So, in general, the constant solution is the only equilibrium in the free-swelling situation, where the gel is simply placed in contact with the bath. So, phase separation cannot be achieved in this situation except transiently through a change of χ achieved, for example, by changing the temperature in the gel.

For $0 < \mathcal{G} = 0.01 < \mathcal{G}_c$, the graph of F has an S shape, first increasing, then decreasing, and finally increasing again as we increase C. Hence, there is a range of $\mu_1 < \mu < \mu_2$, where $F(C) = \mu$ has three equilibria $(C, W) = (C_1, 0)$, $(C_2, 0)$, $(C_3, 0)$, with $C_1 < C_2 < C_3$. The first and the last are saddle points and the middle is a center. As we vary μ, essentially three different phase-plane situations emerge as depicted in Figs. 8(c)–8(e), and these we discuss now.

For one special value $\bar{\mu}$ in the range $\mu_1 < \mu < \mu_2$, the saddle points connect and we have two trajectories between $(C_1, 0)$ and $(C_3, 0)$, which are symmetric upon reflection at the C axis [see Fig. 8(d)]. We can determine this value in the following way. By multiplying (53b) with W on the left-hand side and $(1 + C)^{-1/2} \partial_Z C$ on the right-hand side and integrating over $-\infty < Z < \infty$ we recover the condition for the binodal values (49). For the parameters we use here, we obtain $\bar{\mu} = 6.57 \times 10^{-2}$, $C_1 = 0.800$, and $C_3 = 4.18$ for the chemical potential and the two binodal values, corresponding
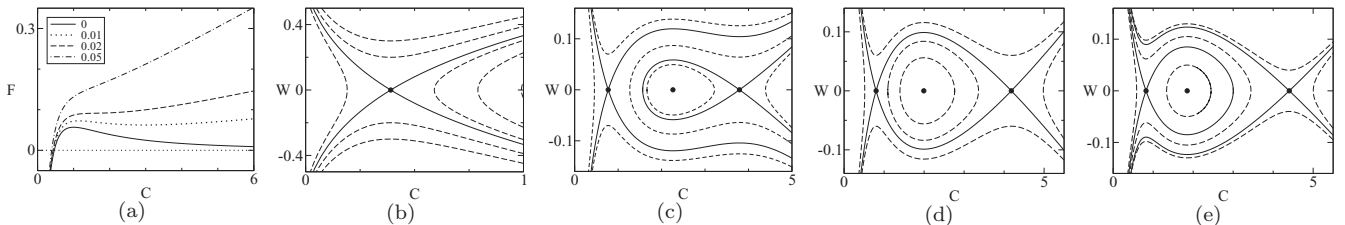
FIG. 8. (a) Graphs of F for $\chi = 1$ and increasing values of $\mathcal{G}$. (b)–(e) Phase planes of (53) when (b) $\chi = 1$, $\mathcal{G} = 0.05$, $\mu = 0$; (c)–(e) $\chi = 1$, $\mathcal{G} = 0.01$ with $\mu_1 < \mu < \bar{\mu}$, $\mu = \bar{\mu}$, and $\bar{\mu} < \mu < \mu_2$, respectively. The values $\bar{\mu}$, μ_1, and μ_2 are explained in the text. Fixed points are emphasized by small circles, trajectories emanating from or asymptoting into fixed points are indicated by solid lines, all other trajectories by dashed lines.

to fluid volume fractions $\phi = 0.444$ and 0.807, respectively. These values are consistent with the two volume fractions to the left and right of the slowly evolving leading front in Fig. 5(a) and match the chemical potential computed from numerical simulations of the full model.

For $\bar{\mu} < \mu < \mu_2$, the left fixed point connects with itself, giving rise to a stationary solution with an isolated spike that tends to the same value C_1 for $Z \to \pm\infty$. This is shown in Fig. 8(e). Inside this homoclinic trajectory, all solutions in the phase plane are periodic, consisting of periodic arrays of spikes. Solutions that arise in the time-dependent simulations display such spikes, but they usually differ in size and are rarely periodic and are hence not stationary. However, when the spikes are well separated, the evolution is slow and can be considered to be quasistationary, except for brief transients where a spike disappears. We therefore expect these spikes to be well approximated by a homoclinic trajectory though the value of μ can be different for each spike. For such a spike solution of (53), we can write a condition that is derived analogously to (49):

$$\int_{C_1}^{C_{\max}} F(C)dC = (C_{\max} - C_1)\mu, \qquad (54)$$

and $F(C_1) = \mu$, where $C_{\max}$ is the maximum value of the spike. These conditions fix μ in terms of the maximum value (or vice versa), and it decreases with $C_{\max}$. Hence, the smaller spikes have a larger potential and this imbalance between the spikes sustains the evolution. As fluid is driven away from the smaller to the larger neighboring spikes, the former shrinks and eventually disappears. This process can be observed, for example, for the middle spike between the last two snapshots in Fig. 6. The corresponding situation occurs for $\mu_1 < \mu < \bar{\mu}$ [see Fig. 8(c)] but with the spikes pointing downward, i.e., appearing as narrow regions where the gel is relatively dry compared to the surroundings.

A special situation arises for $\mathcal{G} = 0$, that is, for vanishing stiffness. For χ above the critical value $\chi_c = \frac{1}{2}$, there are at most two fixed points for $\mu > 0$, and hence front solutions as in the phase plane in Fig. 8(d) never occur. The situation in the phase plane is similar to the one shown in Fig. 8(e), except that the rightmost fixed point is absent. Therefore, in the forced-swelling simulations in Fig. 3(a), the liquid accumulates to a spike right at the left boundary, with an ever-growing maximum $C_{\max}$, that is, with the fluid volume fraction $\phi_f \to 1$. As this happens, the chemical potential μ goes down. For decreasing chemical potential, the far-field value C_1 of the homoclinic solution in the phase plane decreases too [as can be seen from Fig. 8(a) from intersecting the graph of F for $\mathcal{G} = 0$ with horizontal lines at decreasing heights μ]. This is consistent with the behavior in Fig. 3(a), where the fluid never forms a moving front and the fluid volume fraction deeper in the gel is reduced at larger times.

IV. CONCLUSION

In this study we derive a general model for a hydrogel that accounts for finite strain of the polymer network and the contributions to the free energy due to the formation of internal interfacial layers between the phases, together with appropriate boundary conditions at fixed and the free

boundary through which the solvent is transported into (or out of) the polymer network. Based on this model, we investigated uniaxial swelling and deswelling for a range of parameter settings. The model predicts spinodal decomposition for large enough χ, which can in turn be suppressed by larger shear moduli. We predict so-called "spike" solutions representing one-dimensional "droplets" which arise from spinodal decomposition and then undergo coarsening.

Within the unstable regime, the forced intake of solvent induces a volume phase transition by pushing the system into the spinodal region of the phase diagram. This leads to a sharp front, separating highly and weakly swollen phases, that propagates into the gel from the free surface. While a nonzero elastic modulus is required to force the transition front into the gel, for a modulus that is large enough, the formation of this front is suppressed and a swelling mode akin to the gradual transition in the free-swelling case occurs. Interestingly, the front becomes stationary if the flux is switched off, and a second draining front arises if instead the free boundary is set at the constant chemical potential of the bath. Spinodal decomposition can be initiated preferentially near the draining front before it occurs throughout the gel layer, which is followed by coarsening and ejection of highly swollen domains through the free boundary. This ejection of domains has been experimentally observed by Hu *et al.* [16]. Our modeling framework enables this phenomenon to be captured, in contrast to previous theoretical studies which have imposed periodic boundary conditions [21,23].

By treating the Flory-Huggins parameter as a constant, the analysis predicts that volume phase transitions cannot occur under (one-dimensional) free-swelling conditions. However, accurately describing many hydrogel systems requires the use of empirically determined interaction parameters that are concentration dependent. This additional dependence can substantially alter the free-swelling thermodynamics and enable volume phase transitions to occur upon crossing a critical temperature, as observed in PNIPAM-water systems [35]. In this case, the equilibrium free-swelling curve $F(C) = 0$ would pass through the spinodal region of the phase diagram, leading to an interesting situation where free swelling will induce spinodal decomposition. The model presented here is well suited to study such a situation.

Another key feature that determines the swelling thermodynamics is the elastic response of the material. This is affected by the choice of constitutive relationship as well as the allowable modes of deformation. Accurately describing the mechanics of the highly swollen regions that occur upon phase separation, or indeed the conditions for phase separation, may require alternative constitutive equations that extend the neo-Hookean law, such as the Gent law which considers the finite extensibility of polymer chains. Restricting the gel to uniaxial deformations leads to the generation of a large mechanical pressure which was found to suppress the onset of phase separation. By relaxing this restriction, the volumetric expansion will be distributed across the three principal axes, thereby reducing the elastic stresses generated along these directions and hence the mechanical pressure. This could potentially widen the window where phase separation occurs, making this a more robust phenomenon.

It would also be interesting to extend our model to other geometries, in particular, to look at the core-shell structure that forms in spherical beads, and the impact of expansive stresses on the core [15]. In two- and three-dimensional situations involving a gel that is thin compared to its length $h \ll L_0$, we expect additional instabilities to affect, for example, the transition fronts induced by the forced influx of solvent. The volume phase transition produces a bilayer configuration consisting of a highly swollen film that is bonded to a weakly swollen substrate. Such configurations are well known to become unstable [32,36]. For experimental comparisons with the results here, it may be possible to suppress these instabilities by choosing a small enough length scale for the lateral confinement but, in general, corrugations of the one-dimensional solutions will trigger a more complex evolution of the transition boundary. In this context, it would also be exciting to further explore the analogy with lithium intercalation in battery electrodes and the instabilities observed there [37–39]. It would be interesting to know if stress relaxation at the free surface also promotes phase transitions [40] in a swelling hydrogel.

APPENDIX A: SOLVENT TRANSPORT IN EULERIAN COORDINATES

In terms of Lagrangian coordinates X associated with the dry reference state, the equation governing the nominal concentration of solvent C is given by

$$\dot{C} + \nabla_0 \cdot \boldsymbol{j}_0 = 0. \tag{A1}$$

To map (A1) to the corresponding current configuration, we consider the integral form of the balance law, which reads as

$$\frac{d}{dt} \int_{\mathcal{V}_0} C \, dX = -\oint_{\partial \mathcal{V}_0} \boldsymbol{j}_0 \cdot \boldsymbol{N} \, dA, \tag{A2}$$

where $\mathcal{V}_0$ is an arbitrary volume element in the dry state with corresponding (outward) unit normal vector $\boldsymbol{N}$. Using $dx = J \, dX$, Nanson's formula, and the Reynolds transport theorem gives

$$\int_{\mathcal{V}(t)} \left[\frac{\partial c}{\partial t} + \nabla \cdot (c \boldsymbol{v}_n) \right] dx = -\oint_{\partial \mathcal{V}(t)} \boldsymbol{j} \cdot \boldsymbol{n} \, da. \tag{A3}$$

Here, $c = C/J$ and $\boldsymbol{j} = J^{-1} \mathsf{F} \boldsymbol{j}_0$ are the concentration and the flux in the current configuration, respectively, and $\boldsymbol{v}_n = \partial \boldsymbol{x}/\partial t$ is the velocity of the material element initially contained within $\mathcal{V}_0$. The corresponding local balance law in terms of Eulerian coordinates is then

$$\frac{\partial c}{\partial t} + \nabla \cdot (c \boldsymbol{v}_n + \boldsymbol{j}) = 0. \tag{A4}$$

The two contributions in the divergence operator, which sum to give the total solvent flux, represent the fact that solvent is advected with the polymer network and transported down gradients in the chemical potential. Assuming incompressible materials, the solvent volume fraction is given by $\phi_f = vc$, where v is the volume per solvent molecule. Upon multiplying (A4) by v, we can obtain the usual conservation law

$$\frac{\partial \phi_f}{\partial t} + \nabla \cdot (\phi_f \boldsymbol{v}_f) = 0 \tag{A5}$$

by letting the solvent velocity $\boldsymbol{v}_f$ be defined through the relation $\phi_f \boldsymbol{v}_f \equiv \phi_f \boldsymbol{v}_n + v \boldsymbol{j}$. This definition implies that

$$\phi_f (\boldsymbol{v}_f - \boldsymbol{v}_n) = v \boldsymbol{j}. \tag{A6}$$

Using the definition of the flux in (18), we obtain

$$\phi_f (\boldsymbol{v}_f - \boldsymbol{v}_n) = -\frac{D \phi_f}{k_B T} \nabla \mu, \tag{A7}$$

where $D = D_0 (1 - \phi_f)^{-\beta}$ from (26). The Eulerian transport model is completed by linking the network velocity $\boldsymbol{v}_n$ to the displacement $\boldsymbol{u}$ via

$$\frac{\partial \boldsymbol{u}}{\partial t} + (\boldsymbol{v}_n \cdot \nabla) \boldsymbol{u} = \boldsymbol{v}_n, \tag{A8}$$

and using the fact that the deformation gradient tensor is now given by $\mathsf{F}^{-1} = \mathsf{I} - \nabla \boldsymbol{u}$.

APPENDIX B: CALCULATION OF THE KORTEWEG STRESS TENSOR

The Korteweg stress tensor K can be computed directly from the expression

$$\mathsf{K}_{ij} = \frac{1}{J} \frac{\partial \psi_4}{\partial \mathsf{F}_{iK}} \mathsf{F}_{jK}, \tag{B1}$$

where ψ_4 represents the interfacial free energy density. We write ψ_4 in terms of the nominal concentration C as

$$\psi_4 = \frac{\gamma(C)}{2} J |\nabla C|^2. \tag{B2}$$

To calculate the components of K, we use the fact that

$$\frac{\partial}{\partial x_i} = \mathsf{H}_{iJ} \frac{\partial}{\partial X_J}. \tag{B3}$$

Thus, the interfacial energy (B2) can be written as

$$\psi_4 = \frac{\gamma(C)}{2} J \mathsf{H}_{aK} \mathsf{H}_{aL} \frac{\partial C}{\partial X_K} \frac{\partial C}{\partial X_L}. \tag{B4}$$

To evaluate the derivatives of ψ_4 with respect to F, we use

$$\frac{\partial J}{\partial \mathsf{F}_{iK}} = J \mathsf{H}_{iK}, \qquad \frac{\partial \mathsf{H}_{aB}}{\partial \mathsf{F}_{iK}} = -\mathsf{H}_{aK} \mathsf{H}_{iB}. \tag{B5}$$

Then, by using the identity $\mathsf{H}_{aB} \mathsf{F}_{bB} = \delta_{ab}$ and

$$\frac{\partial}{\partial \mathsf{F}_{iJ}} (\mathsf{H}_{aK} \mathsf{H}_{aL}) \mathsf{F}_{lJ} = -\mathsf{H}_{iK} \mathsf{H}_{lL} - \mathsf{H}_{iL} \mathsf{H}_{lK}, \tag{B6}$$

it can be shown that

$$\frac{\partial}{\partial \mathsf{F}_{iJ}} \left(\mathsf{H}_{aK} \mathsf{H}_{aL} \frac{\partial C}{\partial X_K} \frac{\partial C}{\partial X_L} \right) \mathsf{F}_{lJ} = -2 \frac{\partial C}{\partial x_i} \frac{\partial C}{\partial x_l}. \tag{B7}$$

When combining everything, we find that

$$\mathsf{K}_{ij} = \gamma(C) \left(\frac{1}{2} \frac{\partial C}{\partial x_k} \frac{\partial C}{\partial x_k} \delta_{ij} - \frac{\partial C}{\partial x_i} \frac{\partial C}{\partial x_j} \right). \tag{B8}$$

In tensor form, this is equivalent to

$$\mathsf{K} = \gamma(C) \left(\tfrac{1}{2} |\nabla C|^2 \mathsf{I} - \nabla C \otimes \nabla C \right), \tag{B9}$$

which corresponds to (14b).

APPENDIX C: CONTRIBUTIONS TO THE CHEMICAL POTENTIAL FROM COMPOSITION GRADIENTS

The contributions to the chemical potential from gradients in the solvent concentration are given by

$$\mu_G = -\frac{\partial}{\partial X_L}\left(\gamma(C)JH_{iL}H_{iK}\frac{\partial C}{\partial X_K}\right). \qquad (C1)$$

However, this can be simplified by first noting that

$$\mu_G = -\gamma(C)\frac{\partial}{\partial X_L}(JH_{iL})\frac{\partial C}{\partial x_i} - J\nabla\cdot[\gamma(C)\nabla C]. \qquad (C2)$$

Furthermore, the first term on the left-hand side of (C2) can be shown to be zero, i.e.,

$$\frac{\partial}{\partial X_L}(JH_{iL}) = 0. \qquad (C3)$$

To show that (C3) is true, we use the product rule to obtain

$$\frac{\partial}{\partial X_L}\big(JH_{aL}\big) = \frac{\partial J}{\partial X_L}H_{aL} + J\frac{\partial H_{aL}}{\partial X_L}. \qquad (C4)$$

Then, using the identities in (B5), we find that

$$\frac{\partial}{\partial X_L}(JH_{aL}) = J\left(H_{iK}H_{aL}\frac{\partial F_{iK}}{\partial X_L} - H_{aQ}H_{pL}\frac{\partial F_{pQ}}{\partial X_L}\right). \qquad (C5)$$

Now, we can use the equality of mixed second derivatives to write

$$\frac{\partial F_{pQ}}{\partial X_L} = \frac{\partial}{\partial X_L}\left(\frac{\partial x_p}{\partial X_Q}\right) = \frac{\partial}{\partial X_Q}\left(\frac{\partial x_p}{\partial X_L}\right) = \frac{\partial F_{pL}}{\partial X_Q}. \qquad (C6)$$

This gives

$$\frac{\partial}{\partial X_L}(JH_{aL}) = J\left(H_{iK}H_{aL}\frac{\partial F_{iK}}{\partial X_L} - H_{pL}H_{aQ}\frac{\partial F_{pL}}{\partial X_Q}\right) = 0, \qquad (C7)$$

as claimed in (C3).

APPENDIX D: PHASE-PHASE ANALYSIS AND SIMULATIONS WITH A COMPOSITION-DEPENDENT INTERFACIAL ENERGY

The phase-phase analysis carried out in Sec. III D can be generalized to account for composition-dependent interfacial
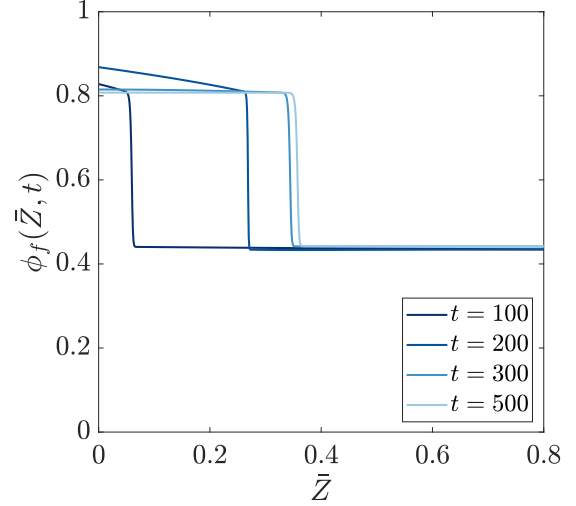
FIG. 9. Numerical simulation of a forced-swelling scenario that is stopped when $t = 200$ after which a no-flux condition is imposed. The parameters are the same as in Fig. 6 except that $\omega = 10^{-4}$ and $\gamma(C) = (1 + C)^{-4}$.

energies $\gamma = \gamma(C)$. The corresponding phase-plane system for the quasistationary solutions of (44) is given by

$$\partial_Z C = (1 + C)^{1/2}W, \qquad (D1a)$$

$$\frac{W}{2}\partial_Z\gamma(C) + \gamma(C)\partial_Z W = (1 + C)^{1/2}(F(C) - \mu), \quad (D1b)$$

which is analogous to (53). The fixed points of (D1) and their linear stability are the same as those of (53). Therefore, the dynamics of (D1) will be qualitatively similar to those illustrated in Fig. 8. Multiplying (D1b) by W results in

$$\tfrac{1}{2}\partial_Z(\gamma(C)W^2) = [F(C) - \mu]\partial_Z C. \qquad (D1c)$$

Integrating (D1c) from $Z = -\infty$ to $+\infty$ produces the same conditions defining the spike solutions given by (54) and the binodal given by (49).

In Fig. 9 we illustrate the effect of using a composition-dependent form of γ in a numerical simulation of a forced-swelling scenario that is stopped when $t = 200$. This situation is analogous to that shown in Fig. 6(a). We take $\gamma(C) = (1 + C)^{-4}$, which corresponds to a (dimensionless) interfacial free energy density given by $\psi_4 = (\omega/2)J|\nabla c|^2$. The qualitative behavior of the solution remains unchanged; however, the diffuse interface separating the two layers is now much thinner, despite the fact that the parameter ω has been increased from 10^{-6} to 10^{-4}.

[1] T. Bertrand, J. Peixinho, S. Mukhopadhyay, and C. W. MacMinn, Phys. Rev. Appl. **6**, 064010 (2016).

[2] C. W. MacMinn, E. R. Dufresne, and J. S. Wettlaufer, Phys. Rev. Appl. **5**, 044020 (2016).

[3] S. Cai and Z. Suo, Europhys. Lett. **97**, 34009 (2012).

[4] T. Gan, Y. Guan, and Y. Zhang, J. Mater. Chem. **20**, 5937 (2010).

[5] J. Krawczyk, S. Croce, T. C. B. McLeish, and B. Chakrabarti, Phys. Rev. Lett. **116**, 208301 (2016).

[6] J. Yoon, S. Cai, Z. Suo, and R. C. Hayward, Soft Matter **6**, 6004 (2010).

[7] M. G. Hennessy, A. Vitale, O. K. Matar, and J. T. Cabral, Soft Matter **13**, 9199 (2017).

[8] T. Tanaka and D. J. Fillmore, J. Chem. Phys. **70**, 1214 (1979).

[9] Y. Li and T. Tanaka, J. Chem. Phys. **92**, 1365 (1990).

[10] M. Engelsberg and W. Barros, Jr., Phys. Rev. E **88**, 062602 (2013).

[11] T. Tanaka, S.-T. Sun, Y. Hirokawa, S. Katayama, J. Kucera, Y. Hirose, and T. Amiya, Nature (London) **325**, 796 (1987).

[12] M. Doi, J. Phys. Soc. Jpn. **78**, 052001 (2009).

[13] K. Dušek and D. Patterson, J. Polymer Sci. Part A-2: Polymer Phys. **6**, 1209 (1968).

[14] T. Tanaka, Phys. Rev. Lett. **40**, 820 (1978).

[15] M. Dušková-Smrčková and K. Dušek, ACS Macro Lett. **8**, 272 (2019).

[16] Z. Hu, C. Wang, Y. Chen, X. Zhang, and Y. Li, J. Polymer Sci. Part B: Polymer Phys. **39**, 2168 (2001).

[17] E. Sato Matsuo and T. Tanaka, J. Chem. Phys. **89**, 1695 (1988).

[18] R. W. Style, T. Sai, N. Fanelli, M. Ijavi, K. Smith-Mannschott, Q. Xu, L. A. Wilen, and E. R. Dufresne, Phys. Rev. X **8**, 011028 (2018).

[19] E. Schuster, K. Sott, A. Ström, A. Altskär, N. Smisdom, T. Gebäck, N. Lorén, and A.-M. Hermansson, Soft Matter **12**, 3897 (2016).

[20] M. S. Dimitriyev, Y.-W. Chang, P. M. Goldbart, and A. Fernández-Nieves, Nano Futures **3**, 042001 (2019).

[21] A. Onuki and S. Puri, Phys. Rev. E **59**, R1331 (1999).

[22] J. Zhou, G. Huang, M. Li, and A. K. Soh, Modell. Simul. Mater. Sci. Eng. **18**, 025002 (2010).

[23] W. Hong and X. Wang, J. Mech. Phys. Solids **61**, 1281 (2013).

[24] A. D. Drozdov, A. A. Papadimitriou, J. H. M. Liely, and C. G. Sanporean, Mech. Mater. **102**, 61 (2016).

[25] P. J. Flory and J. Rehner, J. Chem. Phys. **11**, 512 (1943).

[26] M. E. Gurtin, Physica D (Amsterdam) **92**, 178 (1996).

[27] W. Hong, X. Zhao, J. Zhou, and Z. Suo, J. Mech. Phys. Solids **56**, 1779 (2008).

[28] M. Quesada-Pérez, J. A. Maroto-Centeno, J. Forcada, and R. Hidalgo-Alvarez, Soft Matter **7**, 10536 (2011).

[29] S. A. Chester and L. Anand, J. Mech. Phys. Solids **58**, 1879 (2010).

[30] S. Puri and K. Binder, Phys. Rev. E **66**, 061602 (2002).

[31] Y. Liu, H. Zhang, J. Zhang, and Y. Zheng, Int. J. Solids Struct. **80**, 246 (2016).

[32] M. K. Kang and R. Huang, J. Mech. Phys. Solids **58**, 1582 (2010).

[33] W. Toh, Z. Ding, T. Y. Ng, and Z. Liu, J. Appl. Mech. **82**, 061004 (2015).

[34] F. Afroze, E. Nies, and H. Berghmans, J. Mol. Struct. **554**, 55 (2000).

[35] S. Cai and Z. Suo, J. Mech. Phys. Solids **59**, 2259 (2011).

[36] H. Alawiye, E. Kuhl, and A. Goriely, Philos. Trans. R. Soc., A **377**, 20180076 (2019).

[37] E. Meca, A. Münch, and B. Wagner, Proc. R. Soc. A **472**, 20160093 (2016).

[38] E. Meca, A. Münch, and B. Wagner, Eur. J. Appl. Math. **29**, 118 (2018).

[39] E. Meca, A. Münch, and B. Wagner, Phys. Rev. E **97**, 012801 (2018).

[40] M. Tang and A. Karma, Phys. Rev. Lett. **108**, 265701 (2012).